NSLS-II Beamlines FMX and AMX

The suite of Advanced Beamlines for Biological Investigations with X-rays (ABBIX) at the National Synchrotron Light Source-II (NSLS-II) comprises two macromolecular crystallography (MX) beamlines, the Frontier Macromolecular Crystallography beamline (FMX) and the Highly Automated Macromolecular Crystallography beamline (AMX) (Berman et al., 2011; Schneider et al., 2013; Fuchs et al., 2014). Along with its companion x-ray scattering beamline, LIX, they are scheduled to begin user operation in 2016.

1. INTRODUCTION

Macromolecular crystallography (MX) is undergoing a remarkable transformation driven by biologists, x-ray source developers, and technologists (McSweeney & Fromme, 2014). Structural biologists require both routine and specialized methods to efficiently derive structures from even the smallest crystals, the most fragile and radiation-sensitive ones, and the largest multi-component molecular assemblies. Accelerator physicists continue to perfect the brilliance of advanced synchrotron x-ray beams and introduced the free electron laser sources which led to the invention of serial crystallography from streams of crystals traversing x-ray pulses of unprecedented intensity (Chapman et al., 2011). And detector developers build fast-framing pixel-array detectors (Dinapoli et al., 2011) capable of taking movies of the continuously changing diffraction patterns of crystals rotating in the beam.

FMX and AMX is a pair of MX beamlines that will push the state of the art in x-ray optics and sample delivery and fully exploit the extraordinary high brilliance (photons/s/area/angular divergence/0.1%bandwidth) of NSLS-II undulator beams. Their complementary and overlapping capabilities are designed to meet the needs of the biomedical researcher in revealing structure and function of living systems with best in class instruments for data collections at cryogenic and room temperature, in crystallization media, and by serial crystallographic methods.

Figure 1: The FMX (left) and AMX (center) experimental hutches with their shared first optical enclosure (right) in sector 17-ID at the NSLS-II.

The two MX beamlines share NSLS-II sector 17-ID (Figure 1) and exploit the x-ray spectrum of identical canted in-vacuum undulators (IVU21) of 1.5m length. The microfocusing FMX beamline on the inboard branch employs a two-stage horizontal source demagnification scheme, covers an energy range of 5 – 30 keV (2.5 – 0.4 Å), and at 12.7 keV will focus a flux of ~$5x10^{12}$ ph/s into a spot of 1 μm width; expandable to 50 μm. The companion AMX beamline on the short outboard branch of the sector is optimized for high throughput, is tunable in the range of 5 – 18 keV (2.5 – 0.7 Å), and at 12.7 keV will focus ~10^{13} ph/s into its native focus of 4 μm (h) x 0.3 μm (v); expandable to 100 μm (see Table 1).

1.1 Scientific Mission of FMX

The FMX micro-focusing beamline will produce for macromolecular crystallography the smallest, highest flux-density beam, with low divergence, that NSLS-II can provide. It will be instrumented to exploit this beam, while at the same time being a practical source for more typical problems better suited to a larger beam. Specifically,

- The beamline will address the most difficult problems in MX: small, weakly diffracting crystals, and large unit cells.
- It will produce a tunable energy beam focused down to one micron in dimension with variable divergence controlled by slits.
- It will provide high energy photons to 30 keV to mitigate in conjunction with micro beams radiation damage in especially sensitive crystals.
- The beamline will be flexible enough to provide also a beam in the 50 μm range, reliably achievable through the use of compound refractive lenses or by defocusing its focusing mirrors.
- It will provide cryogenic sample exchange automation at the state of the art as well as room temperature data collection and multi-axis goniometry.
- The station will accommodate frontier experiments to sample multiple micro-crystals in a single setting: serial crystallography.

1.2 Scientific Mission of AMX

The AMX beamline will provide investigators with a highly accessible facility, featuring both automated and remote participation as well as convenient personal access. Exploiting the remarkable source brightness of NSLS-II across a broad energy range, it will be the brightest tunable beamline in its size class for MX in the world, providing high flux with very low divergence. It will support current and emerging styles of data collection and structure solving, and it will have the capacity and flexibility to accommodate new ones made possible by its speed and versatility. The AMX beamline program will address the following objectives:

- Serve crystallographically challenging projects such as large complexes in large unit cells that require use of larger beams to achieve sufficient amplification of diffracted intensity.
- Support programs that require testing of vast numbers of specimens, e.g., studies of membrane proteins, and drug-discovery explorations using specimen at cryogenic temperatures or at room temperature in crystallization plates

- Throughput rates will be so high that the default will be data collection on every specimen: no crystal screening. To support this mode, crystallographic decision making will need to be made by near real-time software assistance.
- Support asynchronous data collections for multiple projects proceeding simultaneously.
- Provide assistance and technology to facilitate remote operation from home institutions.

2. OPPORTUNITIES AFFORDED BY FMX AND AMX

2.1 Micro-beams for finding well-diffracting volumes in heterogeneous crystals

Owing to its unprecedented flux density, FMX will be the premiere beamline for structure determination from crystals that can only be grown to micron size, due to properties of its molecular constituents as is the case with amyloids (Nelson et al., 2005), see Figure 2 or because of the scarcity of the available proteins, as was the case in early studies of G-protein coupled receptors (Warne et al., 2008), see Figure 3.

A further possibility with small beams is to sample a larger crystal, either at equally spaced or pre-chosen points. This can reduce the impact of radiation damage or exploit well diffracting portions of an otherwise bad crystal. Another possibility is to assemble a data set from partial sets, each coming from one of many small crystals.

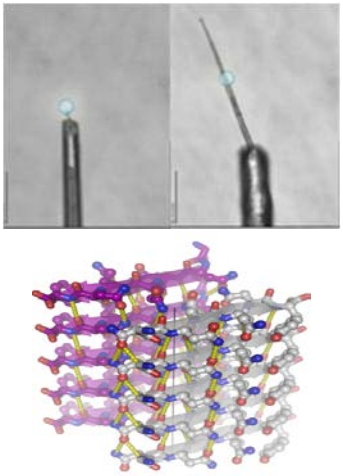

Figure 2: Structure of the cross-ß spine of amyloid-like fibrils (Nelson et al., 2005)

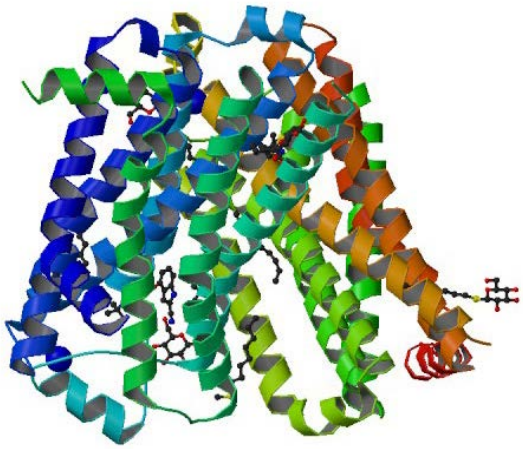

Figure 3: Structure of a ß1-adrenergic G-protein coupled receptor (Warne et al., 2008)

2.2 Tailoring the beam to crystals

2.2.1 Location and ranking of crystals by raster-scanning

Raster scanning of the sample on the goniometer greatly facilitates the centering of hard-to-align samples (Skinner et al., 2006; Aishima et al., 2010; Hilgart et al., 2011). At the FMX and AMX beamlines this indispensable tool will be provided to reliably align small crystals in the presence of precipitate, optical artifacts, or obstructions. Ranking of the crystal's diffraction quality at each raster point can prioritize data collection either automatically or in response to the experimenter's direction.

2.2.2 Crystal morphology mapping

Many crystal shapes make the acquisition of high quality diffraction data hard or impossible. Needle-shaped crystals will yield only high-background data sets if a too-wide beam illuminates buffer along with the crystal itself. Crystals in clusters can be hard to separate, and one may find multiple lattices in the diffraction pattern. Unevenly grown crystals provide data sets averaged over areas with varying mosaicity. One can mitigate each of these problems by a raster-probing of the sample to locate well diffracting areas and to acquire data only from the best crystal volume (Aishima et al., 2010; Bowler et al., 2010).

Strategies to dynamically match beam size and crystal size become essential for micron-sized specimens, since even small mismatches in beam size or position can lead to a scattering volume of buffer equal or larger to that of the crystal. Both FMX and AMX will be equipped with a set of slits for dynamic beam shaping immediately upstream of the crystal location (see Section 3.2.3).

2.2.3 Trajectory-scanning

Closely related to raster-scanning is trajectory-scanning — continuously and synchronously translating and rotating the crystal during the shutter-less data collection. This allows an even distribution of the dose over the useful volume of the crystal. Moreover, for suboptimal crystal morphologies, high quality data can be obtained from evenly grown parts of the crystal by selecting an optimal track through comparably ranked volumes in a preceding raster scan.

2.3 Multi-axis goniometry for optimal crystal orientation and data collection

Multi-axis goniometry opens possibilities for a multitude of optimized data-collection strategies inaccessible to single-axis goniometers. It is possible to reorient crystals from an arbitrary orientation to one optimized for the crystal symmetry and the data-acquisition objective. With an optimized orientation and strategy, the completeness of data acquired can be maximized and the dose can be minimized. More importantly, one can avoid reflection overlaps by aligning long cell axes parallel to the crystallographic rotation axis. For anomalous data collections, the possibility to re-orient crystals to collect Bijvoet pairs on the same frame helps to minimize systematic errors in phasing with SAD/MAD methods.

We plan to implement strategy packages optimized for multi-axis goniometry (Brockhauser et al., 2013). The AMX endstation will be equipped with a SmarGon multi-axis goniometer (SmarAct, Oldenburg, Germany, see Figure 4), an evolution of the PRIGo multiaxis goniometer (Glettig et al., 2011), see Figure 5.

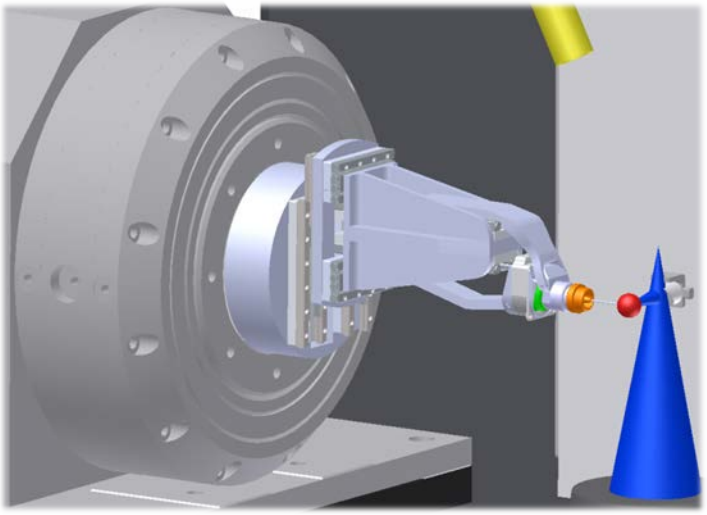

Figure 4: The SmarAct SmarGon multi-axis goniometer mounted on the main goniometer of the AMX experimental station. The sample position is indicated by a red sphere.

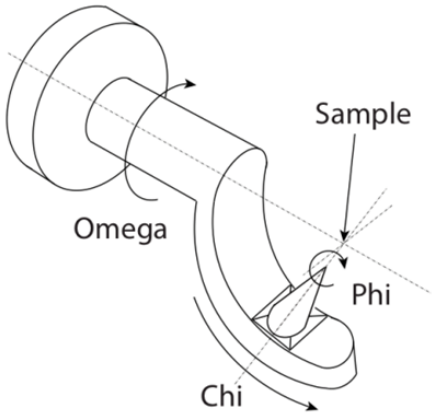

Figure 5: The angular degrees of freedom of the PRIGo / SmarGon multi-axis goniometer are identical to those of a Eulerian cradle.

2.4 Opportunity for multi-crystal and serial crystallography

For very small crystals and for extremely large unit cells, or for a combination of both, one cannot collect a complete data set from a single crystal. Multi-crystal and serial crystallography solve this problem by merging partial data sets from multiple crystals. This approach has been employed early on, for example for the structure solution of whole virus core particles (Grimes et al., 1998).

Multi-crystal crystallography techniques have successfully been established at several beamlines world-wide. In a variant of the method, redundant data sets from multiple 'identical' crystals allowed the selection by hierarchical cluster analysis of the most isomorphous crystals and the merging of the subset to obtain a highly redundant high quality dataset (Liu et al., 2011, 2013; Giordano et al., 2012). We will support serial data collections both with frozen micro crystals on suitable sample supports, as well as at room-temperature in crystallization plates, using protocols similar to those first developed by (Axford et al., 2012). Additionally, the in situ acoustic droplet ejection methods developed by Roessler and Soares (Soares et al., 2011; Roessler et al., 2013) offer intriguing possibilities for rapid specimen delivery and a great increase in throughput of serial data collections.

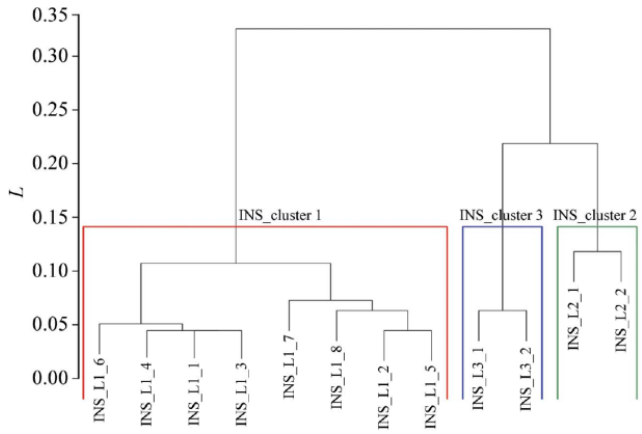

Figure 6: Statistical cluster analysis of redundant experiments for improved phasing and to derive more precise structure factors pioneered by Liu and Hendrickson (Liu et al., 2013) and Giordano et al. (Giordano et al., 2012)

In recent experiments at PETRA-III (Gati et al., 2014) determined the structure of Cathepsin B from a suspension of micron-sized crystals in a single cryo-loop that was systematically scanned in the synchrotron beam in a helical pattern (Figure 7). This data collection approach

implements at the synchrotron the serial femtosecond crystallography experiment developed at the Linac Coherent Light Source where the first Cathepsin B structure was derived (Redecke et al., 2013). A serial experiment at room temperature demonstrated the feasibility of acquiring a dataset from micro crystals flowing through the x-ray beam in a capillary (Stellato et al., 2014), see Figure 8. We will implement established techniques first, and then extend them to address additional challenges stemming from the AMX and FMX beamlines' small beam, small crystal sizes, and high throughput.

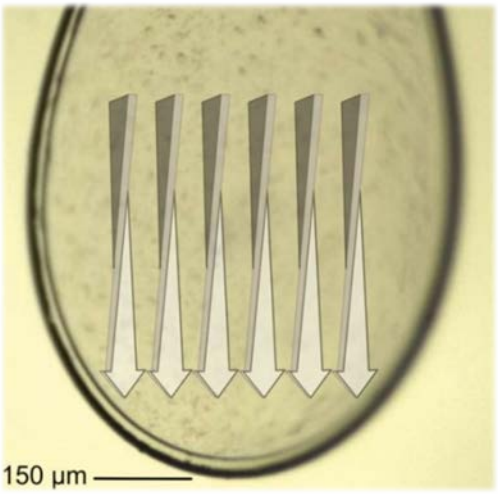

Figure 7: Serial crystallography on in vivo grown microcrystals using synchrotron radiation – frozen crystal suspension at PETRA3 P14 (Gati et al., 2014).

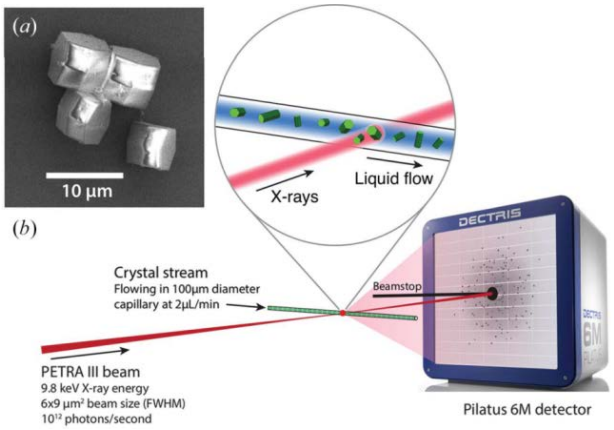

Figure 8: Room-temperature macromolecular serial crystallography using synchrotron radiation – crystal suspension flowing through a capillary at PETRA3 P11 (Stellato et al., 2014)

2.5 Reduced radiation damage from micron beams and high photon energy

X-ray generated photoelectrons are the primary source of radiation damage in macromolecular crystals. If diffraction data are sampled from a volume smaller than the mean path length of the photoelectrons, one can significantly reduce their adverse effect (Cowan & Nave, 2008; Paithankar et al., 2009). Damage rate reductions up to a factor of three upon beam-size changes from 15 to 1 µm (Sanishvili et al., 2011) and of a factor of 4.4 by measurements with a vertical line-focus of 0.7 µm full-width half-maximum (Finfrock et al., 2013) have been reported. At FMX beam shaping and data-collection protocols will be available, e.g. with a vertically extended, but horizontally micron-sized beam, to allow acquisition of datasets using this physical radiation damage mitigation protocol. The effect appears to be more pronounced when photon energy is high (Fourme et al., 2012).

2.6 Asynchronous data collection using automated sample handling

Owing to the high flux at FMX and AMX, specimen throughput eventually can be at least one per minute, a time spent mostly with robotic specimen exchange and automated crystal centering. At these speeds, experimenters will no longer have time to analyze diffraction as it is being measured and to contemplate their next actions. Software will make decisions, or assist experimenters in crystallographic decision making. The experiment will become an asynchronous process where investigators will judge and analyze data that have already been acquired and stored. This leads quite naturally to a new method of allocating beam time to multiple simultaneous users that each get a fraction of the beam time and will have their data collections interleaved with those of others.

The initial objective for FMX and AMX will be to exploit and optimize widely accepted technologies for specimen handling. This will include quick automounters, x-ray-based crystal-centering methods, and robots to measure diffraction from crystals in crystallization plates. The future will be driven by opportunities to create more compact crystal-mounting devices, and flowing-crystal methods.

2.7 Novel crystal handling will connect crystallography labs with synchrotron beamlines

Acoustic droplet ejection (ADE) is a novel technology, employing focused sound waves to transfer specimens directly from the crystallization plates onto data collection media (grids). Alex Soares has already populated grids with a few dozen individually diffracting ~20 μm crystals (Soares et al., 2011) . They yielded a high resolution structure when probed with a 20 μm beam at NSLS-X25 (see Figure 9). The tiny beam and high flux expected at FMX or AMX should allow routine data collection from even smaller crystals on specimen grids prepared using ADE or similar technologies.

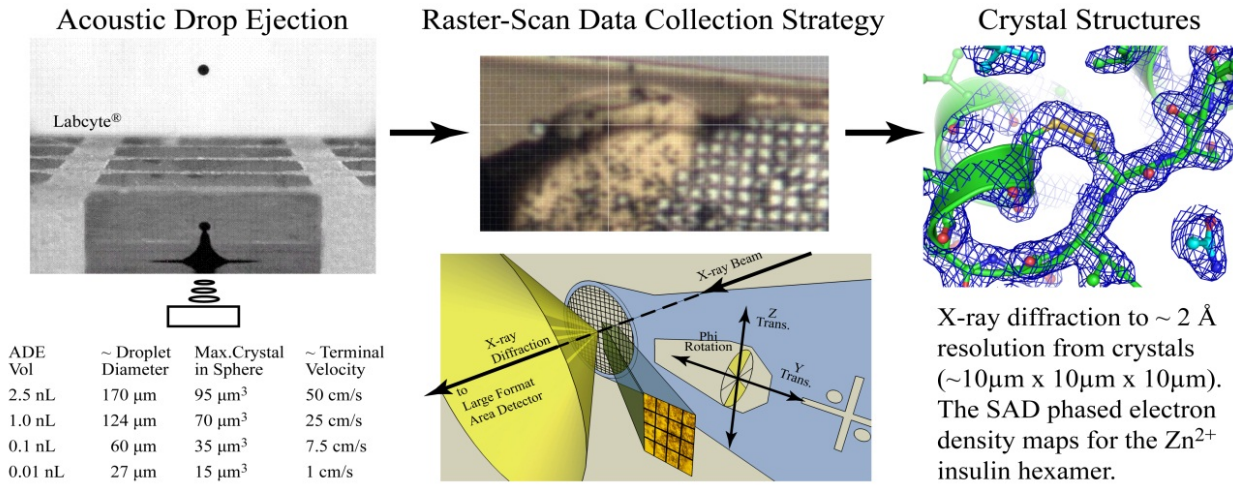

Figure 9: ADE methods launch a 2.5 nL droplet (left), which when caught on a mesh and coupled with a raster-scan data collection (middle), yields crystal structures (right)(Soares et al., 2011).

In cases where the crystallization conditions are well known, a large number of 30–50 μm crystals can be used for chemical biology investigation of a known structure. Soares and colleagues have demonstrated that four individual crystals can be placed on a single mesh and combined with a different chemical (Yin et al., 2014), see Figure 10. When scaled up to 50 unique screening experiments per mesh, large fragment libraries can effectively screened.

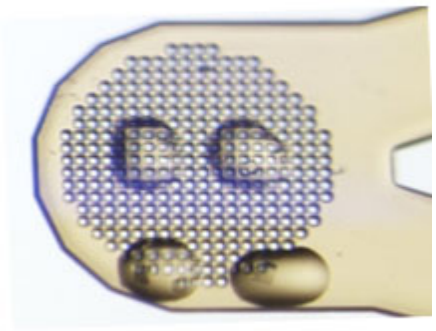

Figure 10: ADE and cryocrystallography high throughput screening: Four crystals in discrete droplets were deposited by ADE and combined with a different drug.

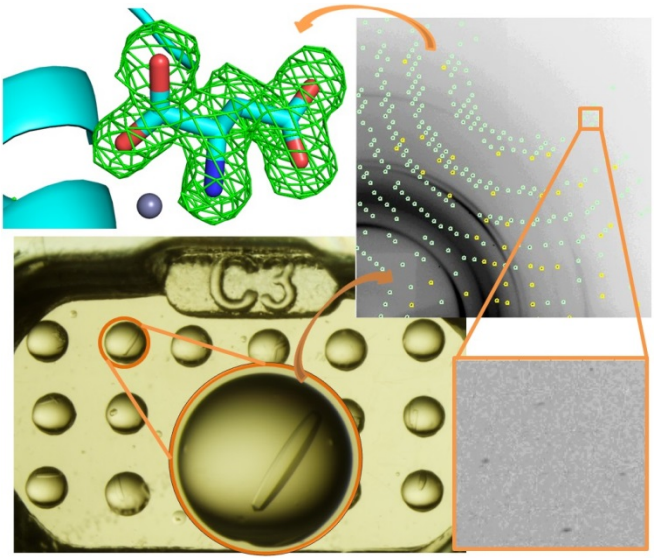

Figure 11: ADE can create crystallization experiments for testing of fragment libraries. Here data were collected with a G-Rob crystallization-tray robot.

2.8 Room temperature data collection at high framing rates

The high data rate of several hundred Hertz possible with modern pixel-array detectors has brought on a renaissance of room-temperature data collection.

Room temperature data collection from crystals in crystallization trays has been shown to allow for structure determination in situations calling for serial crystallography when cryo-protection is not feasible, such as virus crystals (Axford et al., 2012). Recent work has also extended the scope to membrane proteins (Moraes et al., 2014). Further, at room temperature, kinetic processes could be revealed that are be frozen out at cryogenic temperatures.

In addition, in-tray *(in situ*) screening facilitates rapid optimization of crystallization conditions, owing to the elimination of the crystal harvesting step, the cryo protection, and mounting of each crystal (Bingel-Erlenmeyer et al., 2011; Axford et al., 2012).

In combination with high flux density beams, one can sample at extreme dose rates. Previous experiments indicate that there is the possibility to thereby "outrun radiation damage" (Owen et al., 2012, 2014; Warkentin et al., 2013) by recording diffraction before the onset of global radiation damage processes. The extreme intensity available from FMX and AMX will present the ultimate opportunity to verify and possibly perfect this approach.

The integration of the plate handling goniometer into the experimental station is described in section 3.2.7 and in Figure 18.

3. SUMMARY OF FMX AND AMX PERFORMANCE PARAMETERS

3.1 Beamline features and performance

FMX, with its native focal spot of 1 μm and a flux of ~5×10^{12} ph/s at 12.7 keV, will surpass the current brightest MX beamlines by orders of magnitude in achievable dose rates. Its design is

optimized to provide the stability and beam size control required to conduct advanced micro crystallography experiments.

AMX's flux achieves ~10^{13} ph/s at 12.7 keV even at the small vertical beam divergences of 0.3 mrad that structural biologists require for data collection on large unit cell molecular complexes. Its small native focal spot of 4 µm puts AMX in the group of today's best mini-focusing beamlines, and thus among the instruments where one can derive structures expediently from small, oddly shaped, and large unit-cell crystals.

	FMX: Frontier Microfocusing MX	AMX: Highly Automated MX
Source	Canted IVU21 undulator	Canted IVU21 undulator
Optics	Double crystal monochromator (v-axis) Horizontal focusing mirror Horizontal secondary source Compound Refractive Lenses (CRL) Kirkpatrick-Baez focusing mirrors	Double crystal monochromator (h-axis) Tandem deflecting mirrors Kirkpatrick-Baez focusing mirrors
Energy range	5 – 30 keV	5 – 18 keV
Wavelength range	0.4 – 2.5 Å	0.7 – 2.5 Å
Flux at focus	~5 x 10^{12} ph/s	~10^{13} ph/s
Focal spot min	1 x 0.5 µm^2	4 x 3 µm^2
Focal spot range	1 – 50 µm	4 – 100 µm

Table 1: Main components and predicted performance parameters of the FMX and AMX beamlines.

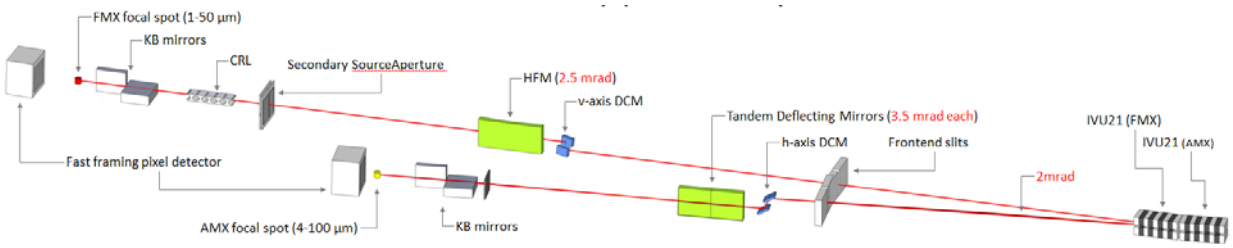

Figure 12: Conceptual layout of the AMX and FMX photon delivery systems. Fed by two canted undulators (IVU21, right), the beamlines share the 17-ID straight section of the NSLS-II storage ring. The long FMX beamline views the inboard-canted downstream undulator, and the short AMX beamline, the outboard-canted upstream undulator. The FMX beamline (top) has a two-stage focusing scheme with a horizontally focusing mirror (HFM) illuminating the secondary source aperture followed by a KB mirror focusing stage. Compound refractive lenses (CRLs) are employed for instant expansion of the FMX beam. FMX's vertical monochromator axis increases vibrational stability. The AMX beamline (bottom) is separated from FMX by tandem side-deflecting mirrors and focused by a single KB-mirror stage.

3.1.1 Energy and beam size selection

Both the photon energy and the beam size can be freely selected by the users. For size selection, bimorph piezo focusing mirrors and, at FMX, an additional compound refractive lens (CRL) stage, will make it possible to effectively tailor the beam size to suit their experiment. As a further option, the focusing mirrors can be taken out of the beam completely to achieve a more parallel beam optimized for crystals with extremely large unit cells.

3.2 Experimental stations features and performance

3.2.1 FMX experimental station

Given FMX's target beam size of 1 µm at unprecedented flux densities, the design of the experimental station of FMX (Figure 13) is strictly optimized for maximal stability. Its central figure of merit is a sphere of confusion (SOC) of the main goniometer working point of less than 10% of the beamline's target beam size – it is designed to achieve a SOC of 100 nm peak to peak upon a full rotation of the main goniometer axis.

To avoid compromising the main goniometer's performance, additional functionalities such as plate-screening or advanced sample mounting techniques such as acoustic droplet ejection are performed on a secondary dedicated goniometer (Figure 18).

Sample microscopy likewise is optimized to the sample and beam spot's micron-sized dimensions. Accompanying location-methods such a diffraction-based rastering and optical fluorescence will be required for cases where purely optical methods fail.

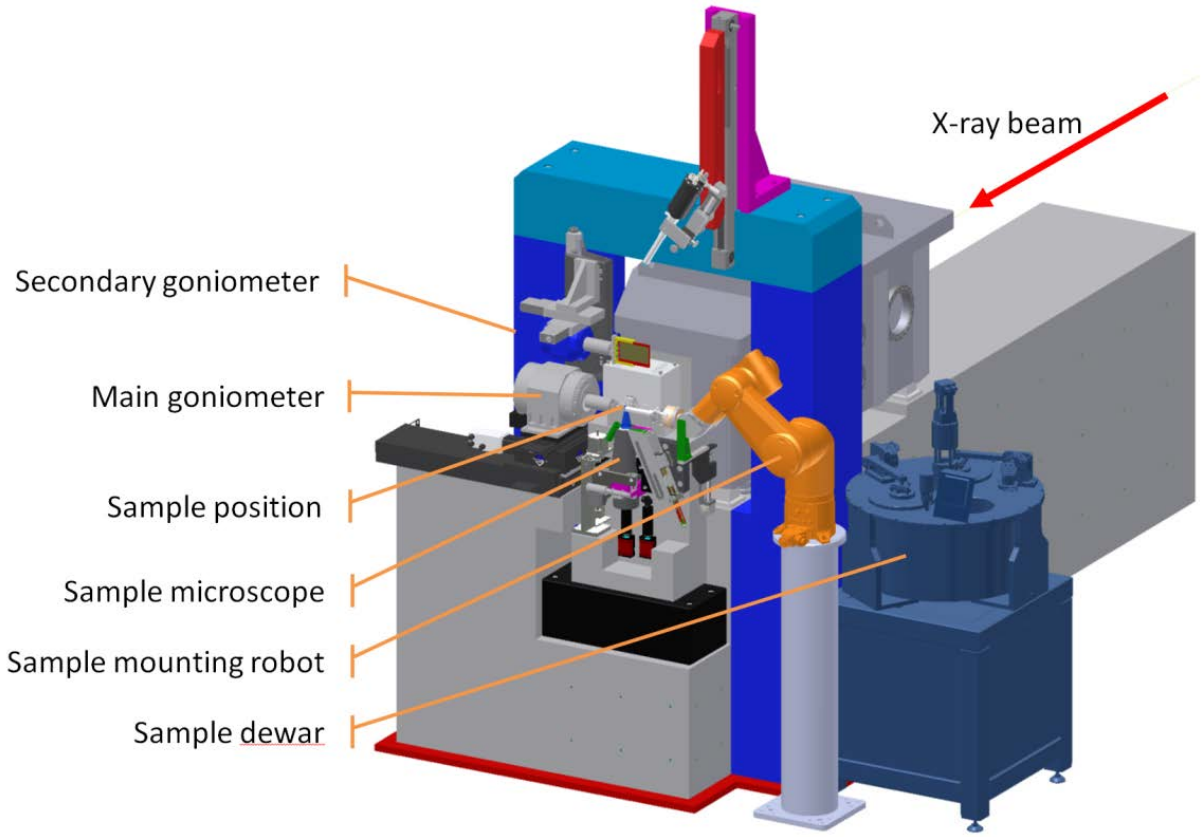

Figure 13: FMX experimental station. The support structure is shared with the focusing KB mirror tank. The main goniometer is shown in working position; the secondary in-plate screening goniometer is parked. A granite arch construction provides support for top mounted components. A six-axis automounter based on a Stäubli TX60 robotic arm mounts samples from the outboard side.

3.2.2 AMX experimental station

The AMX experimental station (Figure 14) is laid out to exploit the high flux, low divergence, and small size of its beam. All high-precision developments for the FMX endstation that fit the experimental space are equally implemented at AMX, such as the high-precision main goniometer, the beam conditioning, and the crystal visualization functionality.

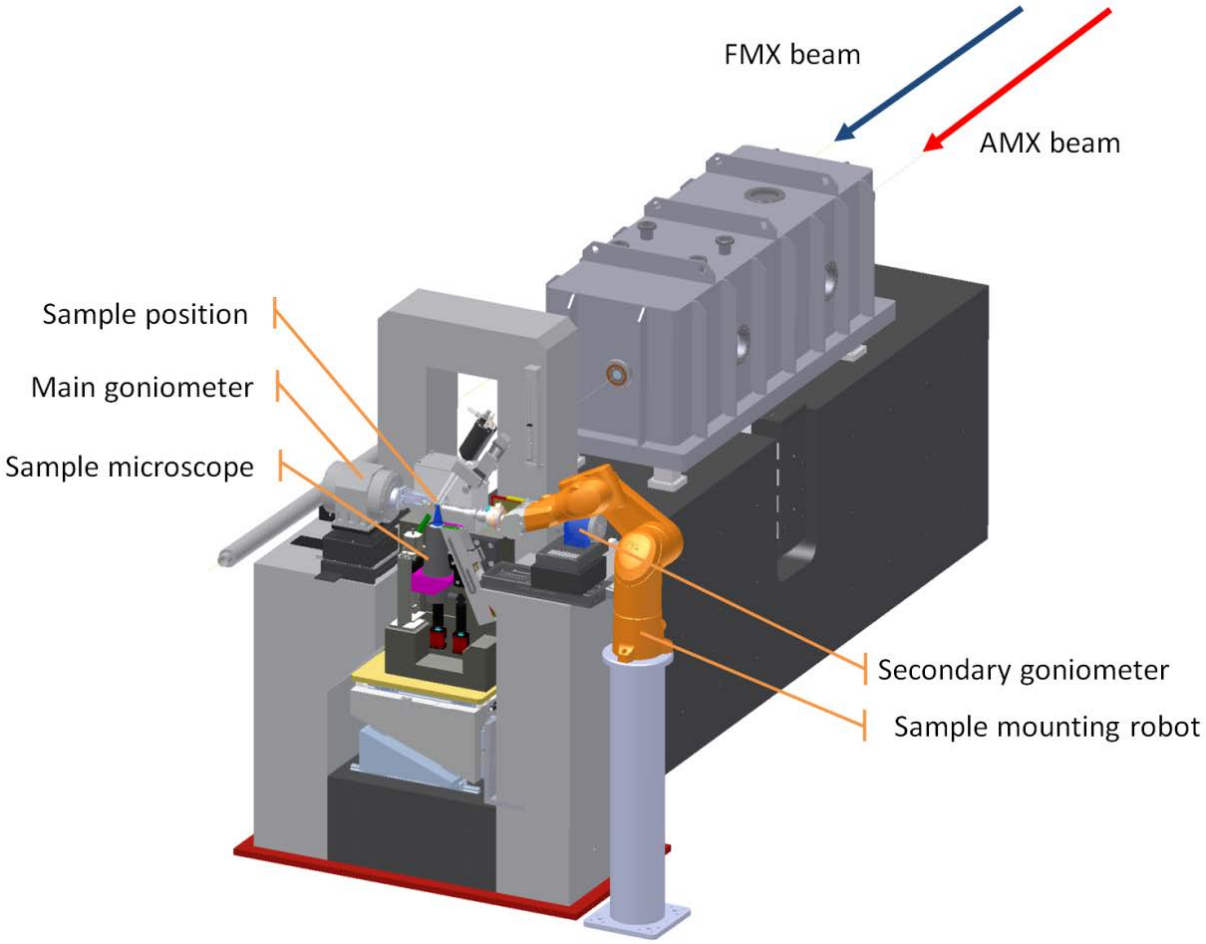

Figure 14: AMX experimental station. the main goniometer is positioned on the inboard side next to the FMX beam pipe, and the automounter on the outboard side. The secondary goniometer is parked outboard and upstream.

3.2.3 Beam conditioning

Piezo slits for dynamic beam shaping: By matching beam size to the crystal's size, one can optimize the signal-to-noise ratio for a given crystal (Nave, 1999). To match the beam size to the crystal size dynamically for an anisotropic crystal shape, the beam size must be changed during the data collection. The FMX and AMX beam conditioning units provide a dynamically adjustable set of piezo-microslits to change the beam size even during open-shutter data collection of few-micron sized crystals.

Beam attenuation and intensity monitoring: Attenuation foil sliders with 4×8 positions provide fine-grained beam intensity selection over the whole photon energy working range from 5 – 30 keV. Continuous intensity monitoring and logging is provided to inform x-ray dose calculation and planning and later data processing.

3.2.4 Beamstop and Helium Path

For mini- and microfocus beamlines, a tight integration of the beam conditioning- and the beamstop units is essential to minimize the background signal from air scatter. With exchangeable sizes and a wide movement range along the beam, FMX and AMX's beamstop can be optimized for micro crystallography, and both for high- and low resolution data collections.

To further minimize air scatter, a He path will be available. The first implementation will be a He filled cone between detector surface and sample position. The final setup will provide

the possibility to purge the complete volume from beam shaping unit to detector surface upon request.

3.2.5 High precision goniometry with advanced scanning modes

To manipulate micro crystals and to support the advanced scanning modes described in section 2.2, high-precision air bearing axes and piezo- and linear motor scanning stages have been integrated into high-precision goniometers. FMX and AMX's main goniometers will provide spheres of confusion and translation precisions of 100 nm, and scanning speeds up to 10 mm/s.

3.2.6 On-axis microscope, crystal visualization

The microscopes at FMX and AMX will be set up to visualize crystals with sizes from 1 mm down to 1 µm. X-ray-based rastering methods will locate crystals; with quick goniometers and fast-framing, low-noise detectors, this process will take only seconds with an attenuated beam, and require minimal x-ray exposure of the specimen. With visible inspection essential for setup and monitoring of a specimen, the following multiple, simultaneous, methods of visible monitoring will be supported: high-quality visible light microscopy with large numerical aperture, UV illumination to produce protein fluorescence, and variable and multi-direction illumination, with multiple microscopes.

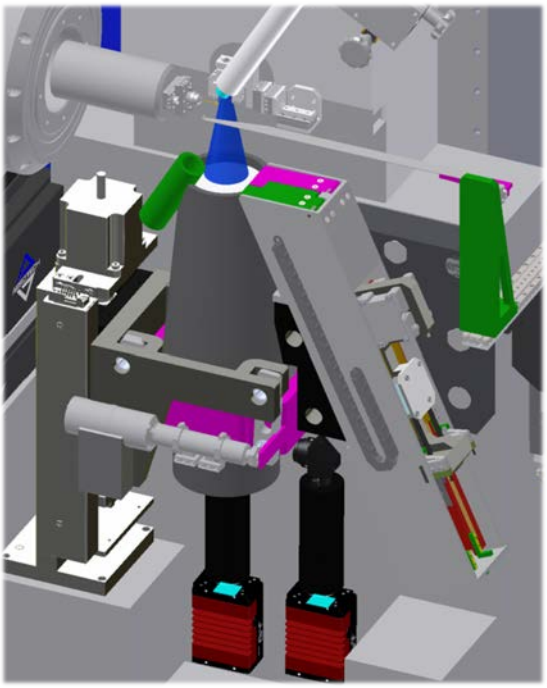

Figure 15: Sample microscope at FMX. The sample is viewed from the x-ray beam direction. The light cone (blue) from the sample is deflected by a mirror to the microscope objective below (grey cone)

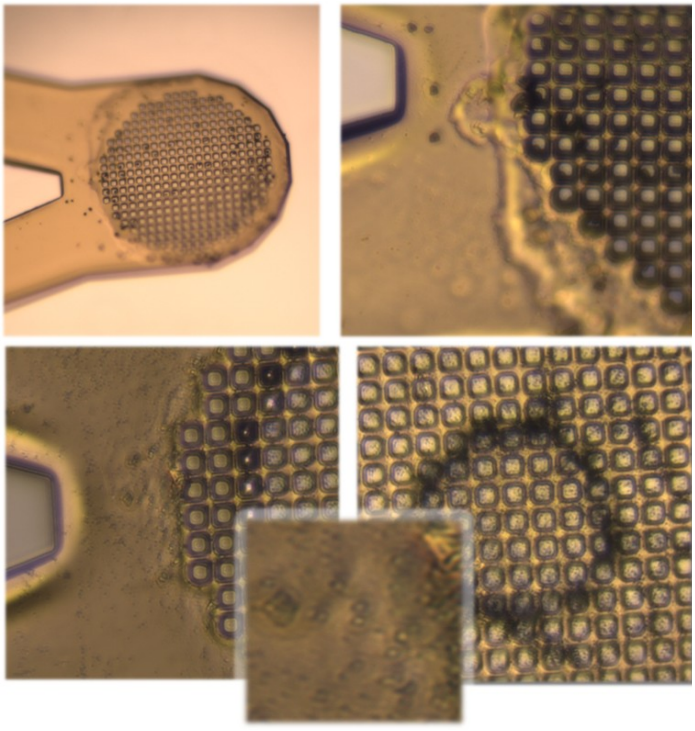

Figure 16: Test images with the Questar QM100 objective demonstrating the high image resolution. Top row: 6 µm size diamond crystals on a sample mesh (pitch 10 µm) at low and high magnification. Bottom row: Same setup with 1 µm size crystals, which are clearly resolved by the objective (insert)

Visual microscopy for sample location and centering becomes challenging for small samples due to image resolution limitations, optical artifacts from buffer and sample support, limited depth of focus at high resolution, and the difficulty to discern crystals from precipitate in the specimen as mounted. The on-axis microscope of the FMX and AMX experimental stations are therefore with additional technologies to improve sample visualization and enhance the information obtained from screening.

The detection and localization of protein crystals can be greatly enhanced by utilizing their intrinsic fluorescence under UV light illumination (Figure 17) (Gofron & Duke, 2010).

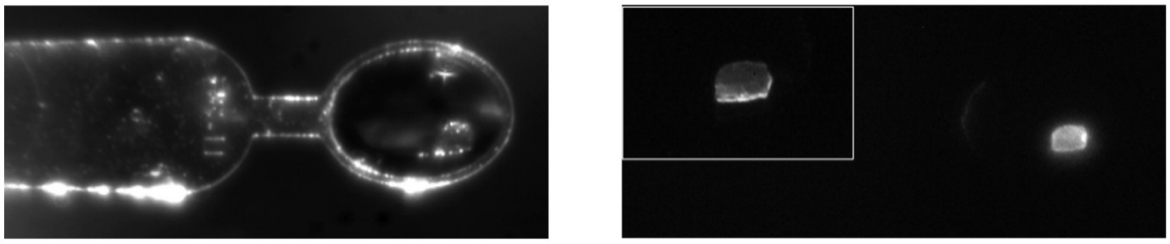

Figure 17: UV light-induced intrinsic fluorescence in a protein crystal used to facilitate detection and localization (Gofron & Duke, 2010).

The expanded beams of AMX and FMX can further be employed to obtain tomographic 3D images of the crystal's shape. This method requires a dose down to well below 1 % of the Henderson limit (Brockhauser et al., 2008), and recent results obtained at beamlines I03 and I04 at the Diamond Light Source suggest that the required dose is significantly smaller than the dose for rastering for crystal location (Warren et al., 2013). We plan to implement this tomography method in an upgrade to the visualization system at the AMX experimental station to enhance automated throughput and establish the minimum useful crystal size.

3.2.7 In-situ plate data collection and screening

To support the crystallization tray data collection laid out in section 2.8, a dedicated plate handling goniometer will be available.

The plate operation at FMX and AMX will be performed on a secondary goniometer axis, which can be brought into the beam automatically and setup within minutes for measurement (Figure 18).

3.2.8 Acoustic Droplet Ejection

We foresee having available the conveyor-belt crystal-delivery apparatus employing Acoustic Droplet Ejection (ADE) (Soares et al., 2011; Roessler et al., 2013). It will be mounted on a dedicated secondary goniometer, to be interchanged automatically with the main goniometer if it is requested.

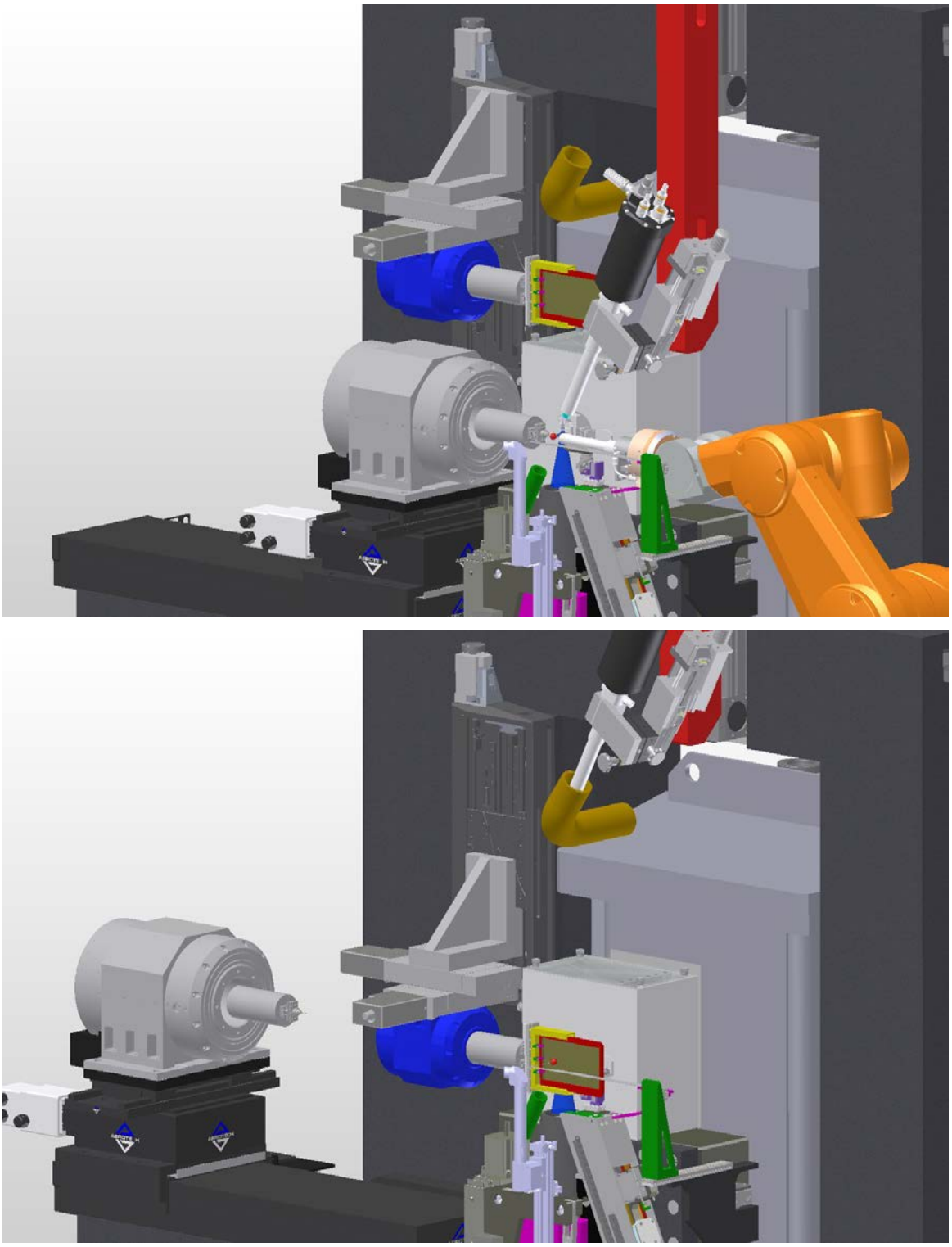

Figure 18: Exchange of main and secondary goniometer to switch from cryo crystallography (top) to plate screening (bottom). The Cryostream nozzle is retracted vertically to the second extraction tube to enable a rapid switch back to cryo operation.

3.2.9 Detector systems

The FMX detector system will be a DECTRIS Eiger X 16M hybrid pixel array detector (HPAD).

As the previous Pilatus HPAD generation (DECTRIS), it operates without readout noise and dark current, has a 1 pixel point spread function, and can be operated in shutter-less mode.

Beyond this, it will feature frame rates of 133 Hz for 16M frame- and 750 Hz for 4M frame readout, a 3 μs dead time, a significantly smaller pixel of 75 μm size in a 4150 × 4371 matrix.

The small pixel size and the noise performance make it an ideal detector for micro crystallography, while the high pixel count is essential in the structure determination from large unit cell crystals. The extreme frame rates will support advanced serial crystallography experiments, rapid rastering evaluations and high flux and time-resolved applications.

For AMX, the Pilatus 6M system of NSLS beamline X25 is upgraded to double its frame rate to 25 Hz. In a later upgrade, we plan to equip AMX with a system comparable to the FMX setup, depending on the technology available then.

The detector support construction will provide translational degrees of freedom in X, Y and Z direction. A 2θ tilt will not be implemented; instead, the Y vertical offset can be used to handle cases where larger Bragg angles shall be recorded. The support will further have motorized yaw and pitch adjustments to optimize the beam normal incidence on the detector surface, which is critical in the measurement of crystals with very large unit cells.

3.2.10 Sample-cooling and temperature control

The default temperature control will be provided by N_2 gas-driven cryocoolers, with a temperature range down to 80 K. In conjunction with the Helium path setup (see below), a possibility to use Helium gas as the cooling agent will be provided.

Lastly, to ensure temperature stability in room temperature measurements, a humidity control device such as the HC1 developed at EMBL Grenoble (Sanchez-Weatherby et al., 2009) can be used.

4. REFERENCES

Aishima, J., Owen, R. L., Axford, D., Shepherd, E., Winter, G., Levik, K., Gibbons, P., Ashton, A., & Evans, G. (2010). *Acta Crystallogr Sect D*. **66**, 1032–1035.

Axford, D., Owen, R. L., Aishima, J., Foadi, J., Morgan, A. W., Robinson, J. I., Nettleship, J. E., Owens, R. J., Moraes, I., Fry, E. E., et al. (2012). *Acta Crystallogr Sect D*. **68**, 592–600.

Berman, L. E., Allaire, M., Chance, M. R., Hendrickson, W. A., Héroux, A., Jakoncic, J., Liu, Q., Orville, A. M., Robinson, H. H., Schneider, D. K., et al. (2011). *Nucl Instr Meth A*. **649**, 131–135.

Bingel-Erlenmeyer, R., Olieric, V., Grimshaw, J. P. A., Gabadinho, J., Wang, X., Ebner, S. G., Isenegger, A., Schneider, R., Schneider, J., Glettig, W., et al. (2011). *Cryst Growth Des*. **11**, 916–923.

Bowler, M. W., Guijarro, M., Petitdemange, S., Baker, I., Svensson, O., Burghammer, M., Mueller-Dieckmann, C., Gordon, E. J., Flot, D., McSweeney, S. M., et al. (2010). *Acta Cryst D*. **66**, 855–864.

Brockhauser, S., Di Michiel, M., McGeehan, J. E., McCarthy, A. A., & Ravelli, R. B. G. (2008). *J Appl Crystallogr*. **41**, 1057–1066.

Brockhauser, S., Ravelli, R. B. G., & McCarthy, A. A. (2013). *Acta Crystallogr. D Biol. Crystallogr.* **69**, 1241–1251.

Chapman, H. N., Fromme, P., Barty, A., White, T. A., Kirian, R. A., Aquila, A., Hunter, M. S., Schulz, J., DePonte, D. P., Weierstall, U., et al. (2011). *Nature*. **470**, 73–77.

Cowan, J. A. & Nave, C. (2008). *J Synchrotron Rad*. **15**, 458–462.

Dinapoli, R., Bergamaschi, A., Henrich, B., Horisberger, R., Johnson, I., Mozzanica, A., Schmid, E., Schmitt, B., Schreiber, A., Shi, X., et al. (2011). *Nucl Instr Meth A*. **650**, 79–83.

Finfrock, Y. Z., Stern, E. A., Alkire, R. W., Kas, J. J., Evans-Lutterodt, K., Stein, A., Duke, N., Lazarski, K., & Joachimiak, A. (2013). *Acta Cryst D*. **69**, 1463–1469.

Fourme, R., Honkimäki, V., Girard, E., Medjoubi, K., Dhaussy, A.-C., & Kahn, R. (2012). *J Appl Cryst*. **45**, 652–661.

Fuchs, M. R., Sweet, R. M., Berman, L. E., Hendrickson, W. A., Chubar, O., Canestrari, N., Idir, M., Yang, L., & Schneider, D. K. (2014). *J Phys Conf Ser*. **493**, 012021.

Gati, C., Bourenkov, G., Klinge, M., Rehders, D., Stellato, F., Oberthür, D., Yefanov, O., Sommer, B. P., Mogk, S., Duszenko, M., et al. (2014). *IUCrJ*. **1**, 87–94.

Giordano, R., Leal, R. M. F., Bourenkov, G. P., McSweeney, S., & Popov, A. N. (2012). *Acta Crystallogr Sect D*. **68**, 649–658.

Glettig, W., Vitins, M., Schwarb, A., Maag, S., & Schulze-Briese, C. (2011). *Proceedings of the 11th Euspen International Conference*, pp. 31–34. Como, Italy: euspen.

Gofron, K. J. & Duke, N. E. C. (2010). *Nucl Instr Meth A*.

Grimes, J. M., Burroughs, J. N., Gouet, P., Diprose, J. M., Malby, R., Zientara, S., Mertens, P. P. C., & Stuart, D. I. (1998). *Nature*. **395**, 470–478.

Hilgart, M. C., Sanishvili, R., Ogata, C. M., Becker, M., Venugopalan, N., Stepanov, S., Makarov, O., Smith, J. L., & Fischetti, R. F. (2011). *J Synchrotron Rad*. **18**, 717–722.

Liu, Q., Liu, Q., & Hendrickson, W. A. (2013). *Acta Cryst D*. **69**, 1314–1332.

Liu, Q., Zhang, Z., & Hendrickson, W. A. (2011). *Acta Cryst D*. **67**, 45–59.

McSweeney, S. & Fromme, P. (2014). *Nature*. **505**, 620–621.

Moraes, I., Evans, G., Sanchez-Weatherby, J., Newstead, S., & Stewart, P. D. S. (2014). *Biochim Biophys Acta Biomem*. **1838**, 78–87.

Nave, C. (1999). *Acta Cryst*. **D55**, 1663–1668.

Nelson, R., Sawaya, M. R., Balbirnie, M., Madsen, A. O., Riekel, C., Grothe, R., & Eisenberg, D. (2005). *Nature*. **435**, 773–778.

Owen, R. L., Axford, D., Nettleship, J. E., Owens, R. J., Robinson, J. I., Morgan, A. W., Doré, A. S., Lebon, G., Tate, C. G., Fry, E. E., et al. (2012). *Acta Cryst D*. **68**, 810–818.

Owen, R. L., Paterson, N., Axford, D., Aishima, J., Schulze-Briese, C., Ren, J., Fry, E. E., Stuart, D. I., & Evans, G. (2014). *Acta Cryst D*. **70**,.

Paithankar, K. S., Owen, R. L., & Garman, E. F. (2009). *J Synchrotron Rad*. **16**, 152–162.

Redecke, L., Nass, K., DePonte, D. P., White, T. A., Rehders, D., Barty, A., Stellato, F., Liang, M., Barends, T. R. M., Boutet, S., et al. (2013). *Science*. **339**, 227–230.

Roessler, C. G., Kuczewski, A., Stearns, R., Ellson, R., Olechno, J., Orville, A. M., Allaire, M., Soares, A. S., & Héroux, A. (2013). *J Synchrotron Rad*. **20**, 805–808.

Sanchez-Weatherby, J., Bowler, M. W., Huet, J., Gobbo, A., Felisaz, F., Lavault, B., Moya, R., Kadlec, J., Ravelli, R. B. G., & Cipriani, F. (2009). *Acta Cryst D*. **65**, 1237–1246.

Sanishvili, R., Yoder, D. W., Pothineni, S. B., Rosenbaum, G., Xu, S., Vogt, S., Stepanov, S., Makarov, O. A., Corcoran, S., Benn, R., et al. (2011). *Proc Natl Acad Sci U A*. **108**, 6127–6132.

Schneider, D. K., Berman, L. E., Chubar, O., Hendrickson, W. A., Hulbert, S. L., Lucas, M., Sweet, R. M., & Yang, L. (2013). *J Phys Conf Ser*. **425**, 012003.

Skinner, J. M., Cowan, M., Buono, R., Nolan, W., Bosshard, H., Robinson, H. H., Héroux, A., Soares, A. S., Schneider, D. K., & Sweet, R. M. (2006). *Acta Crystallogr Sect D*. **62**, 1340–1347.

Soares, A. S., Engel, M. A., Stearns, R., Datwani, S., Olechno, J., Ellson, R., Skinner, J. M., Allaire, M., & Orville, A. M. (2011). *Biochemistry (Mosc.)*. **50**, 4399–4401.

Stellato, F., Oberthür, D., Liang, M., Bean, R., Gati, C., Yefanov, O., Barty, A., Burkhardt, A., Fischer, P., Galli, L., et al. (2014). *IUCrJ*. **1**, 204–212.

Warkentin, M., Hopkins, J. B., Badeau, R., Mulichak, A. M., Keefe, L. J., & Thorne, R. E. (2013). *J Synchrotron Rad*. **20**, 7–13.

Warne, T., Serrano-Vega, M. J., Baker, J. G., Moukhametzianov, R., Edwards, P. C., Henderson, R., Leslie, A. G. W., Tate, C. G., & Schertler, G. F. X. (2008). *Nature*. **454**, 486–492.

Warren, A. J., Armour, W., Axford, D., Basham, M., Connolley, T., Hall, D. R., Horrell, S., McAuley, K. E., Mykhaylyk, V., Wagner, A., et al. (2013). *Acta Crystallogr. D Biol. Crystallogr.* **69**, 1252–1259.

Yin, X., Scalia, A., Leroy, L., Cuttitta, C. M., Polizzo, G. M., Ericson, D. L., Roessler, C. G., Campos, O., Ma, M. Y., Agarwal, R., et al. (2014). *Acta Cryst D*. **70**, 1177–1189.